Consecutive Ruptures on a Complex Conjugate Fault System During the 2018 Gulf of Alaska Earthquake

Shinji Yamashita[1], Yuji Yagi[2], Ryo Okuwaki[2, 3, 4], Kousuke Shimizu[1], Ryoichiro Agata[5], and Yukitoshi Fukahata[6]

[1]Graduate School of Life and Environmental Sciences, University of Tsukuba, Tsukuba, Ibaraki 305-8572, Japan

[2] Faculty of Life and Environmental Sciences, University of Tsukuba, Tsukuba, Ibaraki 305-8572, Japan

[3] Mountain Science Center, University of Tsukuba, Ibaraki 305-8572, Japan

[4] COMET, School of Earth and Environment, University of Leeds, Leeds LS2 9JT, UK

[5] Japan Agency for Marine-Earth Science and Technology, 3173-25 Showa-machi, Kanazawa-ku, Yokohama 236-0001, Japan

[6] Disaster Prevention Research Institute, Kyoto University, Uji, Kyoto 611-0011, Japan

Corresponding author: Shinji Yamashita (syamashita@geol.tsukuba.ac.jp)

Second corresponding author: Yuji Yagi (yagi-y@geol.tsukuba.ac.jp)

Key Points:

- We developed a finite-fault inversion method to estimate rupture evolution and fault geometry for earthquakes rupturing multiple faults
- Our source model of the 2018 Gulf of Alaska earthquake revealed that multiple-rupture stages evolved in a complex conjugate fault system
- Fracture zones on the oceanic floor may have acted as barriers to irregular rupture evolution during the 2018 Gulf of Alaska earthquake

Abstract

We developed a flexible finite-fault inversion method for teleseismic *P* waveforms to obtain a detailed rupture process of a complex multiple-fault earthquake. We estimate the distribution of potency-rate density tensors on an assumed model fault plane to clarify rupture evolution processes, including variations of fault geometry. We applied our method to the 23 January 2018 Gulf of Alaska earthquake, setting the model fault area to fit the distribution of aftershocks occurring within one week of the mainshock. The obtained source model, which successfully explained the complex teleseismic *P* waveforms, shows that the 2018 earthquake ruptured a conjugate system of N-S and E-W faults. The spatiotemporal rupture evolution indicates irregular rupture behavior involving a multiple-shock sequence, which is likely associated with discontinuities in the fault geometry that originated from E-W sea-floor fracture zones and N-S plate-bending faults.

Plain Language Summary

On 23 January 2018, a large earthquake occurred in the Gulf of Alaska offshore from Kodiak Island, rupturing the Pacific tectonic plate seaward of the Alaska-Aleutian trench. This earthquake is known to have had a complex rupture process, with multiple rupture stages in which rupture directions and speeds changed. It has been challenging to adequately explain the observed seismic data, which record complex processes. We developed a method of using seismic data recorded at great distances from the earthquake to estimate rupture evolution and slip direction without making assumptions about fault geometry. We applied our method to the 2018 Gulf of Alaska earthquake. The earthquake process we estimated comprised multiple ruptures that propagated along roughly north-south and east-west trends and was consistent with the aftershock distribution and pre-existing fault zones beneath the sea floor. Our results suggest that the irregular rupture was associated with discontinuities in the fault geometry related to pre-existing subsea fracture zones and bending faults of the Pacific tectonic plate.

1 Introduction

The 23 January 2018 Gulf of Alaska earthquake (moment-magnitude M_W 7.9; U.S. Geological Survey National Earthquake Information Center) struck offshore Kodiak Island (55.9097°N, 149.0521°W, 10.4 km depth; Alaska Earthquake Center, AEC), in the seaward-region of the Alaska-Aleutian subduction zone. The Global Centroid Moment Tensor (GCMT) project (Dziewonski et al., 1981; Ekström et al., 2012) reported that the 2018 Alaska earthquake had strike-slip faulting with a large non-double-couple component (47%). Aftershock seismicity determined by the AEC (USGS, 2017) shows a lineation extending about 120 km N-S near the epicenter and two aftershock clusters centered about 60 km northeast and about 50 km west from the epicenter (Figure 1). The GCMT solutions of aftershocks are dominated by strike-slip faulting, but include normal and reverse faulting (Figure 1).

Several pioneering studies that built finite-fault models based on the aftershock distribution demonstrated that the 2018 Alaska earthquake ruptured a quasi-orthogonal multiple-fault system oriented approximately N-S and E-W (Guo et al., 2020; Hossen et al., 2020; Lay et al., 2018; Ruppert et al., 2018; Zhao et al., 2019). However, it is difficult to adopt a reasonable fault model because the fault model parametrization, number of fault segments, and fault geometries differ by study, partly due to the spatial spread of the aftershock distribution (Figure 1). Based on the static slip distribution estimated from Global Navigation Satellite System and tsunami data, major slips occurred on E-W-striking segments (Hossen et al., 2020; Ruppert et al., 2018; Zhao et al., 2019). Finite-fault inversions estimated that the maximum slip occurred around the boundary between the crust and uppermost mantle in the N-S-oriented segment (Guo et al., 2020; Lay et al., 2018), which would have played a significant role in tsunami generation. However, it remains challenging to adequately explain the complex characteristics of the observed teleseismic body waveforms by conventional finite-fault inversion methods due to the uncertainty on the fault geometry, which lead to significant model errors.

In the framework of finite-fault waveform inversion, uncertainties on the Green's function and fault geometry have been the major sources of model errors (e.g., Duputel et al., 2014; Minson et al., 2013; Ragon et al., 2018; Shimizu et al., 2020; Yagi & Fukahata, 2011). Those due to uncertainty on the Green's function arose from a discrepancy between the true and calculated Green's functions. To mitigate the effect of this uncertainty, Yagi and Fukahata (2011) explicitly introduced the error term of the Green's function into the data covariance matrix. As a result, their inversion framework allowed the stable estimation of the spatiotemporal distribution of slip-rate, usually without the non-negative slip-rate constraint, which had been commonly applied in conventional waveform inversion methods to obtain a plausible solution (e.g., Das & Kostrov, 1990; Hartzell & Heaton, 1983).

Model errors due to uncertainty on the fault geometry arose from inappropriate assumptions about the fault geometry (e.g., Ragon et al., 2018; Shimizu et al., 2020). For strike-slip earthquakes, many seismic stations are distributed in the vicinity of nodal planes where the radiation pattern is sensitive to the assumed fault geometry. An obtained solution can easily be distorted by inappropriate assumptions of strike and dip (Shimizu et al., 2020). These effects can be mitigated by increasing the degrees of freedom in the assumed seismic source model. Shimizu et al. (2020) proposed an inversion method to express slip vectors on the assumed model plane as the seismic potency tensor. Because their method adopts a linear combination of five basis double-couple components (Kikuchi & Kanamori, 1991), the slip direction is not restricted to the two slip components compatible with the fault direction. Of course, the true fault geometry should be compatible with the actual slip direction. Nonetheless, because the teleseismic *P*-wave Green's function is insensitive to slight changes in the absolute source location, their inversion method enabled the spatiotemporal resolution of not only the detailed rupture evolution, but also variation of the focal mechanism, including information on the fault geometry, which may differ from the assumed model plane.

In this study, we developed a flexible finite-fault inversion framework that can estimate both the rupture evolution and focal mechanism of earthquakes that ruptured along multiple complex fault segments. This method incorporates appropriate smoothness constraints and a high-degree-of-freedom planar model into the inversion framework of Shimizu et al. (2020). Application of our framework to the 2018 Alaska earthquake shows that our source model sufficiently reproduced the observed complex waveforms without assumptions on fault geometry. The model also clarified multiple, distinct rupture events in the conjugate fault system that have not been revealed by conventional finite-fault inversion methods.

2 Method

In the inversion framework of Shimizu et al. (2020), the seismic waveform u_j observed at a station j is given by

$$u_j(t) = \sum_{q=1}^{5} \int_S \left(G_{qj}(t,\boldsymbol{\xi}) + \delta G_{qj}(t,\boldsymbol{\xi})\right) * \dot{D}_q(t,\boldsymbol{\xi})\, d\boldsymbol{\xi} + e_{bj}(t), \qquad (1)$$

where G_{qj} is the calculated Green's function of the qth basis double-couple component, δG_{qj} is the model error on G_{qj} (Yagi & Fukahata, 2011), $\dot{D}_q$ is the qth potency-rate density function on the assumed fault model plane S, e_{bj} is background and instrumental noise, $\boldsymbol{\xi}$ represents a position on S, and $*$ denotes the convolution operator in the time domain.

Shimizu et al. (2020) represented the assumed fault model plane S as a rectangle horizontally covering the seismic source region. However, for earthquakes with complex fault geometries, such as the 2018 Alaska earthquake, such a horizontal rectangular model plane includes areas beyond the seismic source region. Therefore, we further extended their inversion framework such that a horizontal non-rectangular model plane can be set according to the shape of the ruptured region as estimated from other information (e.g., aftershock seismicity). In other words, we introduced *a priori* information about the possible ruptured area into the inversion framework. In numerical tests, the use of a non-rectangular model plane improved spatial resolution and computation costs compared to a rectangular one (Text S1 and Figures S1–S4).

In general, inversions are stabilized by adding smoothness constraints either implicitly or explicitly (e.g., Nocquet, 2018; Yabuki & Matsu'ura, 1992). In the formulation of Shimizu et al. (2020), the smoothness constraints on each potency-rate density function $\dot{D}_q$ in space and time are represented as

$$\nabla^2 \dot{D}_q(t,\xi) + \alpha_q = 0, \qquad (2)$$

$$\frac{\partial^2}{\partial t^2} \dot{D}_q(t,\xi) + \beta_q = 0, \qquad (3)$$

where α_q and β_q are assumed to be Gaussian noise with zero mean and covariances of $\sigma^2 \mathbf{I}$ and $\tau^2 \mathbf{I}$, respectively, where $\mathbf{I}$ is an $M \times M$ (M is the number of model parameters) unit matrix. Because they introduced identical Gaussian distributions for all basis components and determined the optimal values of the hyperparameters σ^2 and τ^2 by Akaike's Bayesian information criterion (Akaike, 1980; Yabuki & Matsu'ura, 1992), the potency-rate density functions of basis components with relatively high amplitudes become smoother than those of basis components with relatively low amplitudes, which may bias the solution. Thus, when the amplitudes of the potency-rate density functions differ for each basis component, the standard deviations of the smoothness constraints should depend on the amplitude of each basis component.

In this study, we set the standard deviation of the smoothness constraints for each basis double-couple component to be proportional to its amplitude. That is, instead of α_q and β_q, we directly introduced Gaussian noise with zero mean and covariances $\sigma_q^2 \mathbf{I}$ and $\tau_q^2 \mathbf{I}$, respectively, as

$$\sigma_q^2 \mathbf{I} = k^2 m_q^2 \sigma^2 \mathbf{I}, \qquad (4)$$

$$\tau_q^2 \mathbf{I} = k^2 m_q^2 \tau^2 \mathbf{I}, \qquad (5)$$

where k is a scaling factor and m_q is the total potency of the qth basis double-couple component, which is independently derived from the moment tensor solution. To avoid extremely small standard deviations destabilizing the solution, we adjusted $k|m_q|$ so that it does not fall below 10% of its maximum absolute value. Following Yagi and Fukahata (2011), we determined the hyperparameters σ^2 and τ^2 by Akaike's Bayesian information criterion (Akaike, 1980; Yabuki & Matsu'ura, 1992). In numerical tests, these improved smoothness constraints mitigated the excessive smoothing of the dominant basis component imposed by conventional smoothness constraints and, when combined with a non-rectangular model plane, outperformed the conventional framework (Text S1, Figures S1–S4, Table S1).

3 Data and Fault Parameterization

We used teleseismic P waveforms (vertical components) recorded at stations with epicentral distances of 30–90° (downloaded from the Incorporated Research Institutions for Seismology Data Management Center). Of these, we selected 78 stations with good data quality and azimuthal coverage (Figure 2c) and converted the P waveforms to velocity waveforms at a sampling rate of 0.8 s. The theoretical Green's functions for teleseismic body waves were calculated by the method of Kikuchi and Kanamori (1991) at a sampling rate of 0.1 s, and the attenuation time constraint t^* for the P wave was taken to be 1.0 s. We adopted a 1-D velocity structure derived from the CRUST1.0 model (Laske et al., 2013; Table S2) to calculate the theoretical Green's functions. Following Shimizu et al. (2020), we did not low-pass filter the observed waveforms or calculated Green's functions. For the smoothness constraints, we calculated m_q based on the GCMT solution of the 2018 Alaska earthquake. The GCMT solution shows that the M1 (strike-slip) component is more prominent than the others (Table S3), including the M4 (dip-slip) component (see Figure S4; Kikuchi & Kanamori, 1991). The scaling factor k in eqs. (4) and (5) was set such that $min(k|m_q|) = 1$ (Table S3).

Based on the aftershock distribution, the 2018 Alaska earthquake is considered to have occurred on a quasi-orthogonal multiple-fault system (Guo et al., 2020; Hossen et al., 2020; Lay et al., 2018; Ruppert et al., 2018; Zhao et al., 2019). To cover the high point density area of aftershocks within one week of the event (determined by the AEC; Figure 2a), we set up a non-rectangular horizontal model fault plane with a maximum width and length of 130 km, which was expanded using a bilinear B-spline with a knot spacing of 10 km. We adopted the epicenter as that determined by the AEC: 55.9097°N, 149.0521°W. The depth of the model fault plane was set at 33.6 km according to the GCMT centroid depth. For the inversion analysis, we adopted a potency-rate density function on each knot, each representing a linear combination of B-splines at an interval of 0.8 s. The maximum rupture-front velocity, which defines the rupture starting time at each knot, was set to 7.0 km/s to account for the possibility of supershear rupture propagation. The rupture ending time at each knot was set to 65 s from the origin time based on previous inversion results (Guo et al., 2020; Lay et al., 2018). We evaluated the sensitivity of our model by perturbing the model parameters and comparing our results with those obtained using the conventional smoothness constraints (see Text S2 and Figures S5–S8).

4 Results

We estimated the spatiotemporal distribution of the potency density tensor for the 2018 Alaska earthquake by applying our flexible finite-fault inversion method to teleseismic P waveforms. The estimated total moment tensor, calculated by taking the spatial and temporal integrals of the potency-rate density functions, expresses strike-slip faulting, including 36% non-double-couple components (Figure 2a). The spatial distribution of the potency density tensor, obtained by temporally integrating the potency-rate density functions at each knot, is also dominated by strike-slip focal mechanisms, with a maximum slip of 6 m about 50 km north of the epicenter (Figure 2a). The moment rate function is elevated over two time periods, separated at 27 s from the origin time: the first period is characterized by three large spikes and the second by numerous smaller spikes (Figure 2b). The total seismic moment is 14.9×10^{20} N m (M_W 8.05). The synthetic waveforms from the obtained source model well reproduce the observed waveforms (Figure S10), including those at stations near the nodal planes (Figure 2d).

Based on the moment rate function and snapshots of the potency-rate density tensors (Figures 2b and S11, respectively), we report the detailed rupture history by dividing it into main (A, 0–27 s) and secondary rupture stages (B, 27–65 s). Based on the location, timing, and continuity of the rupture, we further identified three phases (A1–A3) during the main stage and five (B1–B5) during the secondary stage.

4.1 Main Rupture Stage (A)

The initial phase, A1 (0–9 s), started at the hypocenter and propagated bilaterally northward and southward with strike-slip focal mechanisms (snapshot at 2 s in Figure 3a). Although it is generally difficult to identify the preferred fault plane from the two possible nodal planes in this earthquake, the direction of rupture propagation during phase A1 coincided with the N-S directed nodal plane. The spatial distribution of focal mechanisms shows that the strike of the fault plane gradually rotated counterclockwise from north to south of the epicenter; we obtained a strike/dip of 174°/82° around 20 km north of the epicenter, but 163°/76° around 20 km south of the epicenter (6 s in Figure 3a). The northward rupture seems to have stagnated near the 56°N fracture zone (FZ) after about 9 s (Krabbenhoeft et al., 2018).

Phase A2 (7–27 s) started about 50 km northeast of the epicenter at around 7 s after the origin time and propagated west along the Aka FZ (8 s in Figure 3a; Krabbenhoeft et al., 2018). This rupture direction is consistent with the obtained E-W strike directions (e.g., 10 s in Figure 3a). The westward rupture propagated to 149.2°W, where the Aka FZ intersects the N-S aftershock lineation, until 11 s, then turned southward, indicating that the N-S strike direction is the preferred fault plane (12 s in Figure 3a). The southward rupture halted at around 12 s at the same location where the northward rupture of phase A1 had stagnated at about 9 s. After 12 s, a discontinuous rupture occurred along the Aka FZ: ruptures propagating southward and northward from the Aka FZ near 148.6°W are detected at around 16 and 20 s, respectively (Figure 3a). The rupture on the Aka FZ near 149.2°W is again apparent at around 24 s, and gradually ceased by 27 s.

Phase A3 (16–27 s), started about 40 km northwest of the epicenter, near the 56°N FZ, around 16 s after the origin time (Figure 3a). This rupture propagated bilaterally to the northeast and southwest until around 18 s, then gradually abated until around 20 s. At that time, another western rupture occurred at the northwest end of the model region and propagated to the south (20 s in Figure 3a), stagnating at the 56°N FZ about 50 km west of the epicenter at around 22 s (24 s in Figure 3a).

4.2 Secondary Rupture Stage (B)

We identified seven peaks in the moment rate function during the secondary rupture stage (Figure 2b), which we attribute to five phases in the snapshots (Figure 3b). Phase B1 (28–44 s) occurred along the Aka FZ. In particular, phase B1 ruptures at around 32.8 and 40.0 s were relatively large, and appear as individual peaks in the moment rate function (Figures 2b and 3b). Phase B2 (44–52 s) mainly ruptured the region west of the epicenter. The rupture at around 44.8 s occurred along the 56°N FZ and that at around 49.6 s struck about 30 km south of the 56°N FZ (Figure 3b). Phase B3 (53–60 s) occurred mainly northeast of the epicenter, but also struck the intersection of the Aka FZ and the N-S aftershock lineation at around 52.8 s (Figure 3b). A northward rupture from the Aka FZ was also detected at around 57.6 s. The last peak of the moment rate function corresponds to two independent phases that occurred at around 63.2 s: B4 (62–65 s) ruptured about 20 km south of the Aka FZ and B5 (62–64 s) ruptured about 30 km south of the epicenter (Figure 3b).

5 Discussion

Our inversion results indicate that the main rupture stage (0–27 s after origin) affected segments oriented both N-S and E-W, suggesting that the 2018 Alaska earthquake ruptured a conjugate fault system, as proposed in previous studies (Guo et al., 2020; Hossen et al., 2020; Lay et al., 2018; Ruppert et al., 2018; Zhao et al., 2019). Our source model suggests that the rupture occurred along weak zones in the sea floor: fracture zones extending E-W and plate-bending faults parallel to N-S magnetic lineaments (Naugler & Wageman, 1973; Reece et al., 2013). The N-S plate bending faults have been interpreted as pre-existing oceanic spreading features that were reactivated by subduction of the Pacific Plate (Reece et al., 2013). Krabbenhoeft et al. (2018) associated these pre-existing features with the radiation of high-frequency waves based on back-projection and the aftershock distribution.

A notable irregular rupture propagation highlighted by our inversion results is the northward rupture at around 9 s in phase A1 and the southward rupture at around 12 s in phase A2, both of which stopped near the 56°N FZ (8 and 12 s, respectively, in Figure 3a). The N-S aftershock lineation is divided into northern and southern clusters across the 56°N FZ (Figure 3a). Given the phase A1 and A2 ruptures and the geometrical offset of the N-S aftershock lineation, the northern and southern fault system crossing the 56°N FZ can be regarded as a strike-slip step over. Based on our obtained focal mechanisms, these two N-S faults are both right-lateral strike-slip faults that dip steeply to the west (8 and 12 s in Figure 3a), and the counterclockwise rotation of the strike angle during phase A1 is consistent with the southern N-S aftershock lineation (6 s in Figure 3a). Because irregular rupture behaviors are generally a result of geometric complexities, including barriers caused by discontinuous fault steps (e.g., Aki, 1979; Das & Aki, 1977; Harris & Day, 1993), we interpret that this fault step over caused the rupture to stagnate at around 9 and 12 s.

Multiple sub-events occurring in a conjugate strike-slip fault system have been reported in previous studies (Fukuyama et al., 2015; Goldberg et al., 2020; Hudnut et al., 1989; Meng et al., 2012; Ross et al., 2019). In this study, we have shown a causal link between the multiple rupture episodes during the 2018 Alaska earthquake (stages A and B) and pre-existing bathymetric features by resolving both the rupture evolution and variation of fault geometry using only teleseismic body waves. Similar observations were made during the M_W 8.6 2012 Sumatra earthquake in the Wharton basin. That earthquake involved multiple $M_W > 8$ sub-events along a conjugate fault system (Meng et al., 2012; Duputel et al., 2012), which developed by deep ductile shear localization beneath the brittle upper lithosphere of the oceanic plate (Liang et al., 2020).

It is possible that the complex waveforms observed during the 2018 Alaska earthquake were contaminated by reverberations due to the bathymetric setting that cannot be reproduced by the theoretical Green's function, resulting in dummy multiple events (e.g., Fan & Shearer, 2018; Wiens, 1987, 1989; Yue et al., 2017). We evaluated this possibility by using empirical Green's functions (Dreger, 1994; Hartzell, 1978) and confirm that it is unlikely that the multiple rupture stages originated from such reverberations (Text S3 and Figure S9).

The sub-events that occurred after the main A1 phase can be regarded as early aftershocks missing from global catalogs (Fan & Shearer, 2016). Although it is difficult to distinguish whether such early near- to intermediate-field aftershocks were dynamically or statically triggered (Fan & Shearer, 2016), it is noteworthy that the rupture propagated from A1 to A2 at more than 5 km/s (Text S2 and Figure S6); this is faster than the surface wave velocity (3–4 km/s), suggesting that the A2 rupture was triggered by the A1 rupture.

6 Conclusions

Based on the framework of Shimizu et al. (2020), we developed a finite-fault inversion method for teleseismic *P* waveforms with improved smoothness constraints to obtain source processes for earthquakes with complex multiple-fault ruptures. We applied our inversion method to the 2018 Alaska earthquake and estimated its spatiotemporal rupture process. Although the observed waveforms are very complicated, reflecting the complex rupture process and fault geometry, the waveforms calculated from our source model fit well. The obtained source model suggests a complex multiple-shock sequence on a conjugate fault system, consistent with pre-existing bathymetric features. Irregular rupture stagnation about 20 km north of the epicenter may have been promoted by a fault step across a sea-floor fracture zone.

Acknowledgments

We thank the editor and the reviewers for evaluating the manuscript. This work was supported by the Grant-in-Aid for Scientific Research (C) 19K04030. The facilities of IRIS Data Services, and specifically the IRIS Data Management Center, were used for access to waveforms, related metadata, and/or derived products used in this study. IRIS Data Services are funded through the Seismological Facilities for the Advancement of Geoscience (SAGE) Award of the National Science Foundation under Cooperative Support Agreement EAR-1851048. All the figures were generated with matplotlib (v3.1.1: https://doi.org/10.5281/zenodo.3264781) (Hunter, 2007), ObsPy (1.1.0: https://doi.org/10.5281/zenodo.165135) (Beyreuther et al., 2010) and Generic Mapping Tools (Wessel et al., 2013).

Data Availability Statement

Waveform data was downloaded through the IRIS Wilber 3 system (https://ds.iris.edu/wilber3/find_stations/10607586). Teleseismic waveforms were obtained from the following networks: the Canadian National Seismograph Network (CN; https://doi.org/10.7914/SN/CN); the Caribbean USGS Network (CU; https://doi.org/10.7914/SN/CU); the GEOSCOPE (G; https://doi.org/10.18715/GEOSCOPE.G); the Hong Kong Seismograph Network (HK; https://www.fdsn.org/networks/detail/HK/); the New China Digital Seismograph Network (IC; https://doi.org/10.7914/SN/IC); the IRIS/IDA Seismic Network (II; https://doi.org/10.7914/SN/II); the International Miscellaneous Stations (IM; https://www.fdsn.org/networks/detail/IM/); the Global Seismograph Network (IU;

https://doi.org/10.7914/SN/IU), and the Pacific21 (PS; https://www.fdsn.org/networks/detail/PS/). The moment tensor solutions are obtained from the GCMT catalog (https://www.globalcmt.org/CMTsearch.html). The CRUST 1.0 model is available at https://igppweb.ucsd.edu/~gabi/crust1.html. The fracture zone data is obtained from the Global Seafloor Fabric and Magnetic Lineation Data Base Project website (http://www.soest.hawaii.edu/PT/GSFML/).

References

Akaike, H. (1980). Likelihood and the Bayes procedure. *Trabajos de Estadistica Y de Investigacion Operativa* **31,** 143–166. https://doi.org/10.1007/BF02888350

Aki, K. (1979). Characterization of barriers on an earthquake fault. *Journal of Geophysical Research: Solid Earth*, *84*(B11), 6140-6148. https://doi.org/10.1029/JB084iB11p06140

Beyreuther, M., Barsch, R., Krischer, L., Megies, T., Behr, Y., & Wassermann, J. (2010). ObsPy: A Python toolbox for seismology. *Seismological Research Letters*, *81*(3), 530-533. https://doi.org/10.1785/gssrl.81.3.530

Bird, P. (2003). An updated digital model of plate boundaries. *Geochemistry, Geophysics, Geosystems*, *4*(3). https://doi.org/10.1029/2001GC000252

Das, S., & Aki, K. (1977). Fault plane with barriers: a versatile earthquake model. *Journal of geophysical research*, *82*(36), 5658-5670. https://doi.org/10.1029/JB082i036p05658

Das, S., & Kostrov, B. V. (1990). Inversion for seismic slip rate history and distribution with stabilizing constraints: Application to the 1986 Andreanof Islands earthquake. *Journal of Geophysical Research: Solid Earth*, *95*(B5), 6899-6913. https://doi.org/10.1029/JB095iB05p06899

Dreger, D. S. (1994). Empirical Green's function study of the January 17, 1994 Northridge, California earthquake. *Geophysical research letters*, *21*(24), 2633-2636. https://doi.org/10.1029/94GL02661

Duputel, Z., Agram, P. S., Simons, M., Minson, S. E., & Beck, J. L. (2014). Accounting for prediction uncertainty when inferring subsurface fault slip. *Geophysical Journal International*, *197*(1), 464-482. https://doi.org/10.1093/gji/ggt517

Duputel, Z., Kanamori, H., Tsai, V. C., Rivera, L., Meng, L., Ampuero, J. P., & Stock, J. M. (2012). The 2012 Sumatra great earthquake sequence. *Earth and Planetary Science Letters*, *351*, 247-257. https://doi.org/10.1016/j.epsl.2012.07.017

Dziewonski, A. M., Chou, T. A., & Woodhouse, J. H. (1981). Determination of earthquake source parameters from waveform data for studies of global and regional seismicity. *Journal of Geophysical Research: Solid Earth*, *86*(B4), 2825-2852. https://doi.org/10.1029/JB086iB04p02825

Ekström, G., Nettles, M., & Dziewoński, A. M. (2012). The global CMT project 2004–2010: Centroid-moment tensors for 13,017 earthquakes. *Physics of the Earth and Planetary Interiors*, *200*, 1-9. https://doi.org/10.1016/j.pepi.2012.04.002

Fan, W., & Shearer, P. M. (2016). Local near instantaneously dynamically triggered aftershocks of large earthquakes. *Science*, *353*(6304), 1133-1136. https://doi.org/10.1126/science.aag0013

Fan, W., & Shearer, P. M. (2018). Coherent seismic arrivals in the P wave coda of the 2012 MW 7.2 Sumatra earthquake: Water reverberations or an early aftershock?. *Journal of Geophysical Research: Solid Earth*, *123*(4), 3147-3159. https://doi.org/10.1002/2018JB015573

Fukuyama, E. (2015). Dynamic faulting on a conjugate fault system detected by near-fault tilt measurements. *Earth, Planets and Space*, *67*(1), 1-10. https://doi.org/10.1186/s40623-015-0207-1

GEBCO Compilation Group (2020) GEBCO 2020 Grid (doi:10.5285/a29c5465-b138-234d-e053-6c86abc040b9)

Goldberg, D. E., Melgar, D., Sahakian, V. J., Thomas, A. M., Xu, X., Crowell, B. W., & Geng, J. (2020). Complex rupture of an immature fault zone: A simultaneous kinematic model of the 2019 Ridgecrest, CA earthquakes. *Geophysical Research Letters*, *47*(3), e2019GL086382. https://doi.org/10.1029/2019GL086382

Guo, R., Zheng, Y., An, C., Xu, J., Jiang, Z., Zhang, L., ... & Wen, Y. (2020). The 2018 Mw 7.9 offshore Kodiak, Alaska, earthquake: An unusual outer rise strike‐slip earthquake. *Journal of Geophysical Research: Solid Earth*, *125*(5), e2019JB019267. https://doi.org/10.1029/2019JB019267

Harris, R. A., & Day, S. M. (1993). Dynamics of fault interaction: Parallel strike‐slip faults. *Journal of Geophysical Research: Solid Earth*, *98*(B3), 4461-4472. https://doi.org/10.1029/92JB02272

Hartzell, S. H. (1978). Earthquake aftershocks as Green's functions. *Geophysical Research Letters*, *5*(1), 1-4. https://doi.org/10.1029/GL005i001p00001

Hartzell, S. H., & Heaton, T. H. (1983). Inversion of strong ground motion and teleseismic waveform data for the fault rupture history of the 1979 Imperial Valley, California, earthquake. *Bulletin of the Seismological Society of America*, *73*(6A), 1553-1583.

Hossen, M. J., Sheehan, A. F., & Satake, K. (2020). A multi-fault model estimation from tsunami data: An application to the 2018 M7. 9 Kodiak earthquake. *Pure and Applied Geophysics*, 1-12. https://doi.org/10.1007/s00024-020-02433-z

Hudnut, K., Seeber, L., Rockwell, T., Goodmacher, J., Klinger, R., Lindvall, S., & McElwain, R. (1989). Surface ruptures on cross-faults in the 24 November 1987 Superstition Hills, California, earthquake sequence. *Bulletin of the Seismological Society of America*, *79*(2), 282-296.

Hunter, J. D. (2007). Matplotlib: A 2D graphics environment. *Computing in science & engineering*, *9*(3), 90-95. https://doi.org/10.1109/MCSE.2007.55

Kikuchi, M., & Kanamori, H. (1991). Inversion of complex body waves—III. *Bulletin of the Seismological Society of America*, *81*(6), 2335-2350.

Krabbenhoeft, A., von Huene, R., Miller, J. J., Lange, D., & Vera, F. (2018). Strike-slip 23 January 2018 MW 7.9 Gulf of Alaska rare intraplate earthquake: Complex rupture of a fracture zone system. *Scientific reports*, *8*(1), 1-9. https://doi.org/10.1038/s41598-018-32071-4

Laske, G., Masters, G., Ma, Z., & Pasyanos, M. (2013, April). Update on CRUST1. 0—A 1-degree global model of Earth's crust. In *Geophys. Res. Abstr* (Vol. 15, p. 2658).

Lay, T., Ye, L., Bai, Y., Cheung, K. F., & Kanamori, H. (2018). The 2018 MW 7.9 Gulf of Alaska earthquake: Multiple fault rupture in the Pacific plate. *Geophysical Research Letters*, *45*(18), 9542-9551. https://doi.org/10.1029/2018GL079813

Liang, C., Ampuero, J. P., & Pino Muñoz, D. (2020). Deep ductile shear localization facilitates near-orthogonal strike-slip faulting in a thin brittle lithosphere. https://doi.org/10.31223/osf.io/fp8xq

Matthews, K. J., Müller, R. D., Wessel, P., & Whittaker, J. M. (2011). The tectonic fabric of the ocean basins. *Journal of Geophysical Research: Solid Earth*, *116*(B12). https://doi.org/10.1029/2011JB008413

Meng, L., Ampuero, J. P., Stock, J., Duputel, Z., Luo, Y., & Tsai, V. C. (2012). Earthquake in a maze: Compressional rupture branching during the 2012 Mw 8.6 Sumatra earthquake. *Science*, *337*(6095), 724-726. https://doi.org/10.1126/science.1224030

Minson, S. E., Simons, M., & Beck, J. L. (2013). Bayesian inversion for finite fault earthquake source models I—Theory and algorithm. *Geophysical Journal International*, *194*(3), 1701-1726. https://doi.org/10.1093/gji/ggt180

Naugler, F. P., & Wageman, J. M. (1973). Gulf of Alaska: Magnetic anomalies, fracture zones, and plate interaction. *Geological Society of America Bulletin*, *84*(5), 1575-1584. https://doi.org/10.1130/0016-7606(1973)84<1575:GOAMAF>2.0.CO;2

Nocquet, J. M. (2018). Stochastic static fault slip inversion from geodetic data with non-negativity and bound constraints. *Geophysical Journal International*, *214*(1), 366-385. https://doi.org/10.1093/gji/ggy146

Ragon, T., Sladen, A., & Simons, M. (2018). Accounting for uncertain fault geometry in earthquake source inversions–I: theory and simplified application. *Geophysical Journal International*, *214*(2), 1174-1190. https://doi.org/10.1093/gji/ggy187

Reece, R. S., Gulick, S. P., Christeson, G. L., Horton, B. K., van Avendonk, H., & Barth, G. (2013). The role of farfield tectonic stress in oceanic intraplate deformation, Gulf of Alaska. *Journal of Geophysical Research: Solid Earth*, *118*(5), 1862-1872. https://doi.org/10.1002/jgrb.50177

Ross, Z. E., Idini, B., Jia, Z., Stephenson, O. L., Zhong, M., Wang, X., ... & Hauksson, E. (2019). Hierarchical interlocked orthogonal faulting in the 2019 Ridgecrest earthquake sequence. *Science*, *366*(6463), 346-351. https://doi.org/10.1126/science.aaz0109

Ruppert, N. A., Rollins, C., Zhang, A., Meng, L., Holtkamp, S. G., West, M. E., & Freymueller, J. T. (2018). Complex faulting and triggered rupture during the 2018 MW 7.9 offshore Kodiak, Alaska, earthquake. *Geophysical Research Letters*, *45*(15), 7533-7541. https://doi.org/10.1029/2018GL078931

Shimizu, K., Yagi, Y., Okuwaki, R., & Fukahata, Y. (2020). Development of an inversion method to extract information on fault geometry from teleseismic data. *Geophysical Journal International*, *220*(2), 1055-1065. https://doi.org/10.1093/gji/ggz496

U.S. Geological Survey Earthquake Hazards Program. (2017). Advanced National Seismic System (ANSS) Comprehensive Catalog of Earthquake Events and Products. https://doi.org/10.5066/F7MS3QZH

Wessel, P., Matthews, K. J., Müller, R. D., Mazzoni, A., Whittaker, J. M., Myhill, R., & Chandler, M. T. (2015). Semiautomatic fracture zone tracking. *Geochemistry, Geophysics, Geosystems*, *16*(7), 2462-2472. https://doi.org/10.1002/2015GC005853

Wessel, P., Smith, W. H., Scharroo, R., Luis, J., & Wobbe, F. (2013). Generic mapping tools: improved version released. *Eos, Transactions American Geophysical Union*, *94*(45), 409-410. https://doi.org/10.1002/2013EO450001

Wiens, D. A. (1987). Effects of near source bathymetry on teleseismic P waveforms. *Geophysical Research Letters*, *14*(7), 761-764. https://doi.org/10.1029/GL014i007p00761

Wiens, D. A. (1989). Bathymetric effects on body waveforms from shallow subduction zone earthquakes and application to seismic processes in the Kurile trench. *Journal of Geophysical Research: Solid Earth*, *94*(B3), 2955-2972. https://doi.org/10.1029/JB094iB03p02955

Yabuki, T., & Matsu'Ura, M. (1992). Geodetic data inversion using a Bayesian information criterion for spatial distribution of fault slip. *Geophysical Journal International*, *109*(2), 363-375. https://doi.org/10.1111/j.1365-246X.1992.tb00102.x

Yagi, Y., & Fukahata, Y. (2011). Introduction of uncertainty of Green's function into waveform inversion for seismic source processes. *Geophysical Journal International*, *186*(2), 711-720. https://doi.org/10.1111/j.1365-246X.2011.05043.x

Yue, H., Castellanos, J. C., Yu, C., Meng, L., & Zhan, Z. (2017). Localized water reverberation phases and its impact on backprojection images. *Geophysical Research Letters*, *44*(19), 9573-9580. https://doi.org/10.1002/2017GL073254

Zhao, B., Qi, Y., Wang, D., Yu, J., Li, Q., & Zhang, C. (2019). Coseismic slip model of the 2018 M w 7.9 Gulf of Alaska earthquake and its seismic hazard implications. *Seismological Research Letters*, *90*(2A), 642-648. https://doi.org/10.1785/0220180141

References From the Supporting Information

Lawson, C. L., & Hanson, R. J. (1974). *Solving least squares problems,* Prentice-Hall, Englewood Cliffs., New Jersey.

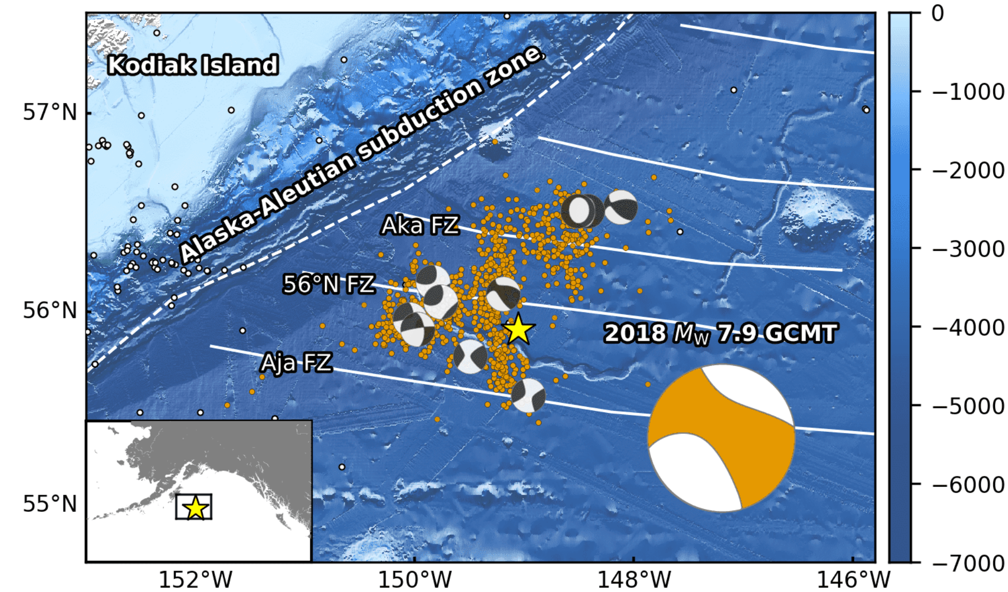

Figure 1. Overview of the source region of the 2018 Gulf of Alaska earthquake. The star is the mainshock epicenter, orange dots are aftershocks ($M \geq 3$) that occurred within one week of the mainshock, and white dots show background seismicity before the mainshock ($M \geq 3.5$, 1 January 2008 to 22 January 2018); all epicentral locations are from AEC. The 'beachball' diagrams show the GCMT solutions for the mainshock (large, bottom right) and aftershocks with $M \geq 3.5$. White dashed lines represent plate boundaries (Bird, 2003), and white solid lines represent fracture zones (Matthews et al., 2011; Wessel et al., 2015). The background bathymetry is derived from the GEBCO 2020 Grid (GEBCO Compilation Group, 2020). The inset map shows the regional setting.

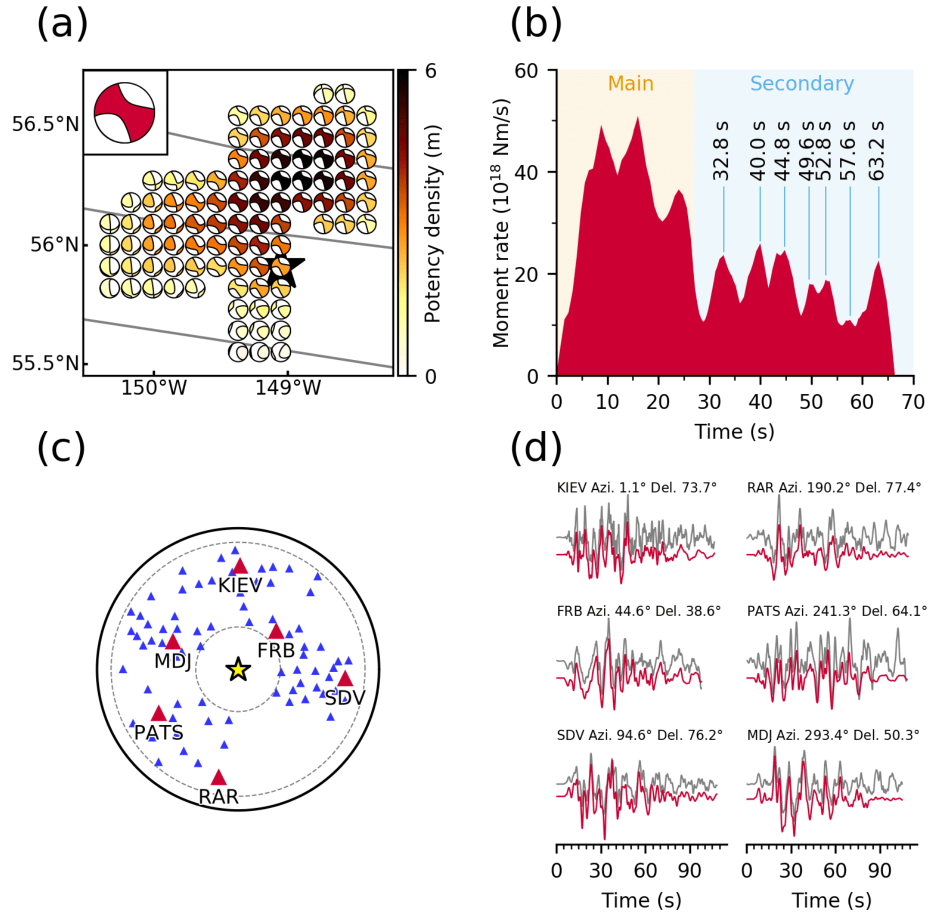

Figure 2. Model setting and summary of results. (a) Map projection of the potency density tensor distribution on the assumed model fault plane. The star and solid lines indicate the epicenter (AEC) and fracture zones (Matthews et al., 2011; Wessel et al., 2015), respectively. Inset is the total moment tensor. (b) The moment rate function is divided into the main and secondary rupture stages at 27 s. The individual peaks during the secondary stage correspond to snapshots in Figure 3b. (c) Azimuthal equidistant projection of the station distribution used in the inversion. The star denotes the epicenter, and triangles denote station locations (waveforms for red stations are shown in (d)). The inner and outer dotted lines show epicentral distances of 30° and 90°, respectively. (d) Comparison of observed waveforms (gray) with synthetic waveforms (red) at the selected stations in (c). Each panel is labeled with the station name, azimuth (Azi.), and epicentral distance (Del.) from the mainshock. Waveform comparisons for all stations are shown in Figure S10.

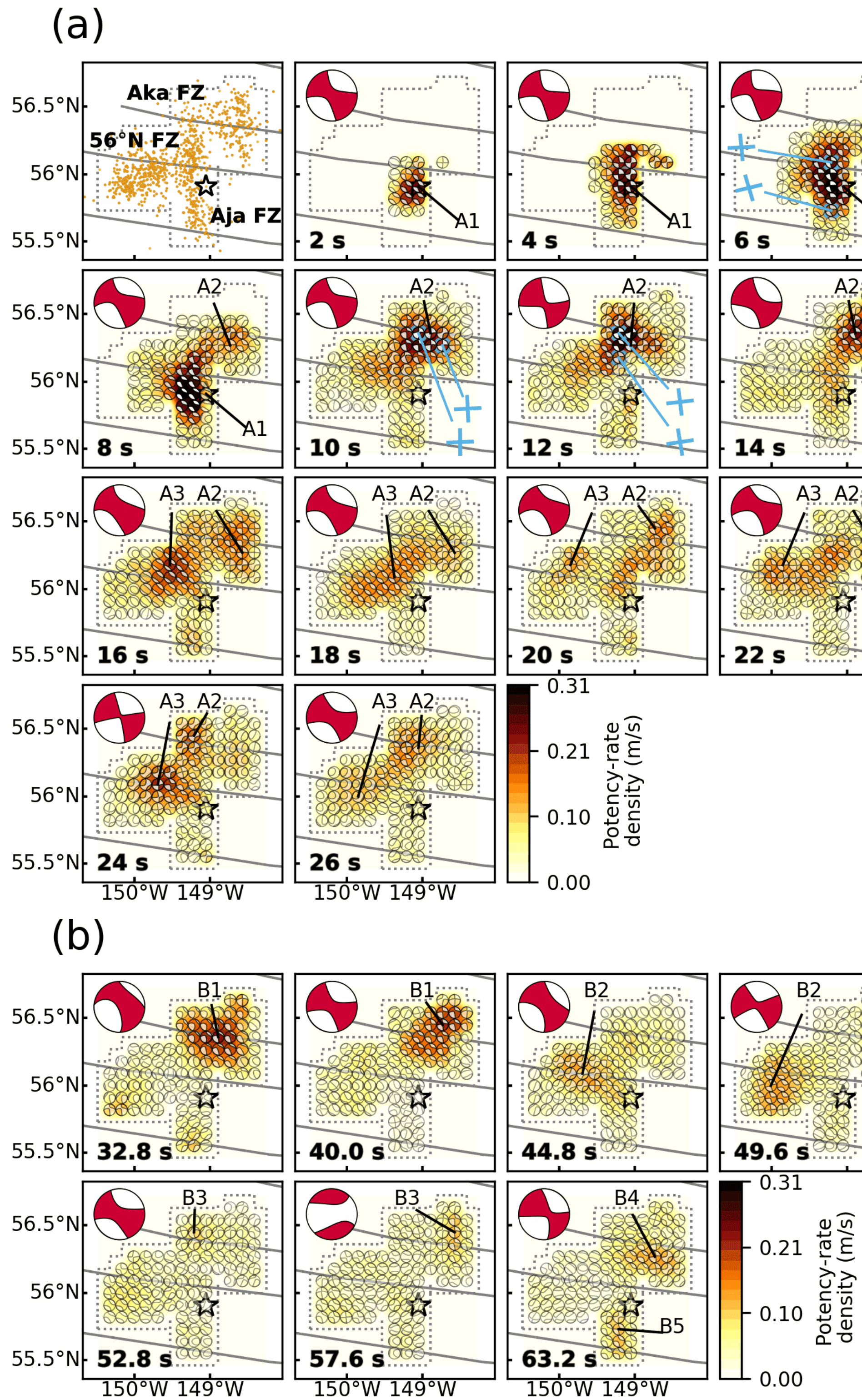

Figure 3. Snapshots of the potency-rate density tensors for (a) the main rupture stage A and (b) the secondary rupture stage B. The corresponding time after onset for each snapshot is noted at the bottom-left of each panel. The dotted line shows the border of the assumed model fault plane.

The star and solid lines indicate the epicenter (AEC) and fracture zones (Matthews et al., 2011; Wessel et al., 2015), respectively. Blue crosses show the strike directions of small beachball diagrams derived from the potency-rate density tensor. The top-left panel in (a) is the epicentral distribution of aftershocks ($M \geq 3$) that occurred within one week of the mainshock (AEC). The large beachball in each panel indicates the corresponding total moment tensor at each time.